Check for updates

A Sodium–Antimony–Telluride Intermetallic Allows Sodium-Metal Cycling at 100% Depth of Discharge and as an Anode-Free Metal Battery

Yixian Wang, Hui Dong,* Naman Katyal, Hongchang Hao, Pengcheng Liu, Hugo Celio, Graeme Henkelman, John Watt, and David Mitlin*

Repeated cold rolling and folding is employed to fabricate a metallurgical composite of sodium–antimony–telluride $Na_2(Sb_{2/6}Te_{3/6}Vac_{1/6})$ dispersed in electrochemically active sodium metal, termed "NST-Na." This new intermetallic has a vacancy-rich thermodynamically stable face-centered-cubic structure and enables state-of-the-art electrochemical performance in widely employed carbonate and ether electrolytes. NST-Na achieves 100% depth-of-discharge (DOD) in 1 M $NaPF_6$ in G2, with 15 mAh cm^{-2} at 1 mA cm^{-2} and Coulombic efficiency (CE) of 99.4%, for 1000 h of plating/stripping. Sodium-metal batteries (SMBs) with NST-Na and $Na_3V_2(PO_4)_3$ (NVP) or sulfur cathodes give significantly improved energy, cycling, and CE (>99%). An anode-free battery with NST collector and NVP obtains 0.23% capacity decay per cycle. Imaging and tomography using conventional and cryogenic microscopy (Cryo-EM) indicate that the sodium metal fills the open space inside the self-supporting sodiophilic NST skeleton, resulting in dense (pore-free and solid electrolyte interphase (SEI)-free) metal deposits with flat surfaces. The baseline Na deposit consists of filament-like dendrites and "dead metal", intermixed with pores and SEI. Density functional theory calculations show that the uniqueness of NST lies in the thermodynamic stability of the Na atoms (rather than clusters) on its surface that leads to planar wetting, and in its own stability that prevents decomposition during cycling.

1. Introduction

Sodium metal holds considerable promise as an anode material for Na-based batteries, considering its high capacity of 1166 mAh g^{-1} and low redox potential of −2.71 V versus standard hydrogen electrode (SHE).[1] Dendrite growth is ubiquitous when electroplating a wide range of metals in a similarly wide range of electrolytes.[2] Dendrite growth is well recognized as the major impediment to implementation of metal anodes for both Na and Li batteries.[3] Sodium-metal anodes are hampered by somewhat analogous issues as Li anodes but to a worse extent: repeated electrodeposition/electrostripping of Na is accompanied by concurrent dendrite growth and unstable solid electrolyte interphase (SEI). This in turn leads to a series of major issues, including a marked rise in cell impedance, low Coulombic efficiency (CE), electrolyte exhaustion, and premature cell failure that may be catastrophic. For example, SEI-induced electrolyte depletion[4] and dendrite growth through the battery separator[5] are well-documented. Significant gains have been achieved in promoting stable dendrite-free cycling of Li-metal anodes.[6] In contrast, cycling stability with Na-metal anodes remains more limited due to its greater reactivity in battery electrolytes.

Both Li and Na metal occupy a higher energy level compared with the lowest unoccupied molecular orbital (LUMOs) of organic electrolytes. Since the number of electron shells in Na is larger than in Li, there is a lower constraining force on the outermost electrons. This causes Na to be a more reductive agent than Li in comparable electrolytes.[7] Sodium also possesses 55% larger ionic radius than Li,[8] and has a notably weaker bonding with solid carbon resulting in less exothermic adsorption/intercalation.[9] In carbonate- or ether-based solvents, Na metal is more reactive than Li metal when tested under identical conditions. These include various combinations of carbonates such as ethylene carbonate (EC), propylene carbonate (PC), diethyl carbonate (DEC), and dimethyl carbonate (DMC), as well as ethers such as dimethoxyethane (DME), diglyme (G2),

Y. Wang, H. Dong, H. Hao, P. Liu, H. Celio, D. Mitlin
Materials Science and Engineering Program & Texas Materials Institute (TMI)
The University of Texas at Austin
Austin, TX 78712-1591, USA
E-mail: hdong@utexas.edu; david.mitlin2@utexas.edu

N. Katyal, G. Henkelman
Department of Chemistry
The University of Texas at Austin
Austin, TX 78712, USA

J. Watt
Center for Integrated Nanotechnologies
Los Alamos National Laboratory
Los Alamos, NM 87545, USA

and tetraglyme (G4). Compared to Li metal, Na-metal anodes in ether and ester solvents possess accelerated SEI growth, worse CE, larger overpotentials for plating and stripping, and more severe growth of dendrites.[10] The morphology of Na dendrites is varied but is often described as "needle-like," "filament-like," or "mossy."[11] In the case of Li, these shapes are associated with defect-catalyzed base growth conditions at currents low enough where ion-diffusional limitations do not yet dominate.[12] Likely, this is also the case for Na dendrites, although the role of SEI in the growth morphology requires further analysis.

To address above challenges, numerous strategies have been proposed, such as formation of SEI film in situ by adding electrolyte additives,[13] fabrication of an artificial protection layer on the Na-metal surface,[14] construction of 3D hosts for Na metal,[15] and regulation of Na deposition by controlling the nucleation sites.[16] Creating sodiophilic surfaces to promote metal wetting during deposition and in parallel reduce the nucleation/growth overpotentials has been shown to be highly effective. For example, Huang's group reported an inspirational strategy for improving the sodiophilicity and lowering Na^+ diffusion barrier by the spontaneous reaction between molten Na and SnO_2, with the formation of a percolated dual-conductive Na–Sn alloy/Na_2O skeleton.[17]

In most studies improved Na plating/stripping performance is demonstrated using unrealistically thick anodes, for example, 300 µm to 1 mm foils. Such thick anode foils contribute inactive metal to the weight and the volume of the battery. Thick metal anodes also pose an increased safety risk due to the overall larger amount of reactive metal. For research applications, however, a relatively low depth-of-discharge (DOD) of several percent will give a more favorable assessment of the cell cycling performance. The plating–stripping volume changes (relative to the total anode thickness) are less, and there is always fresh metal to compensate for ongoing SEI formation and other sources of CE loss. A survey of state-of-the-art Na-metal anode literature showed that a typical DOD was less than 5% of the overall metal-foil capacity.[18] A volume change of 5% is less disruptive to the anode and to the SEI than the oft-quoted infinite volume change corresponding to 100% DOD. More challenging configuration-based deep cycling conditions and respectively greater DOD have been proposed as the research path forward.[16a] One method to study deep discharge/charge (stripping/plating) is to employ "anodeless"/"anode-free" configurations where the active ions are stored entirely in the cathode while the anode is effectively a blank current collector.[19] This of course results in 100% DOD per cycle and represents the most challenging configuration. Another method to achieve a large DOD is to employ thin foils, e.g., 50 µm, with aggressive cycling in terms of plated/stripped capacities. It should also be pointed out that thin (25–50 µm range) Na-metal anodes are needed for commercially viable NMBs. While such Na foils are currently not available, this serves as the appropriate target for future development efforts.

In this study, three electrolyte solutions were employed: 1 M NaFSI in EC/DEC (1:1, v/v), 1 M $NaClO_4$ in EC/PC (1:1, v/v) with 5 wt% FEC, and 1 M $NaPF_6$ in G2. Carbonates are the existing commercial choice and widely used in ion-battery research due their oxidation stability that allows for high-voltage cathode materials.[20] In addition, the solubility of Na polysulfides in carbonates is lower than that in ethers. Room-temperature Na–S batteries generally deliver better cycling stability in carbonate-based electrolytes due to the suppression of the polysulfide shuttling.[21] Carbonate-based electrolytes however pose a major challenge for Na-metal anodes due to the severe side reactions and the formation of nonuniform and irregular SEI.[22] An electrolyte solution based on 1 M $NaPF_6$ in G2 has been demonstrated to allow for a more stable SEI formed on plating/stripping sodium anodes, the SEI being rich in Na_2O and NaF phases near the metal surface.[10c,22b,23] The scientific impact of this work may be subdivided into a fabrication-testing aspect and an analytical science aspect. First, there is a novel synthesis route that creates a new thermodynamically stable ternary intermetallic. When utilized as a metal anode support, this intermetallic allows for among the most favorable planting/stripping performances reported in the literature. The second impact of this work is an in-depth mechanistic description regarding the interdependence of cluster and atom adsorption energies, metal film wetting behavior and dendrites, SEI growth, and the resultant electrochemical stability or instability. To achieve this new insight, a combined analytical (including cryo-focused ion beam (FIB), cryo-scanning electron microscopy (SEM), and cryo-transmission electron microscopy (TEM)) and simulation (density functional theory (DFT)) approach was employed. The fact that the findings are consistent with three commonly employed sodium-metal electrolytes, rather than with some novel formulation, makes the results broadly applicable.

2. Results and Discussion

Extended details of the electrode fabrication, electrochemical analysis, characterization, and simulations are provided under the "Experimental and Simulation" section in the Supporting Information. In summary, a sodium antimony telluride intermetallic–Na metal composite, termed "NST-Na," was fabricated by repeated rolling and folding of antimony telluride (Sb_2Te_3) powder and Na metal inside an Ar-filled glove box (<0.1 ppm H_2O and O_2 level). The 20 iterations of repeated rolling and folding resulted in the in situ formation of a metallurgical composite structure consisting of stable sodium antimony tellurium crystallites densely dispersed within an electrochemically active Na-metal matrix. As per the DFT simulation of the structure and the indexed X-ray diffraction (XRD) pattern, NST is a new ternary vacancy-rich ordered intermetallic compound $Na_2(Sb_{2/6}Te_{3/6}Vac_{1/6})$ based on the face-centered-cubic (fcc) Na_2Te structure. **Scheme 1** illustrates the rolling and folding process, which was repeated 20 times to create a foil ≈150 µm in thickness. The digital photographs show top-down and cross-sectional views of the resultant self-standing foil. The images were taken with a cell phone while the foil remained in the argon-filled glove box. It may be observed that its surface is macroscopically smooth, its shiny luster indicating minimum oxidation. Figure S1a in the Supporting Information illustrates the two configurations employed for battery assembly and testing. Configuration 1 is NST-Na or NST (Na-metal-stripped) electrodes being supported by a standard stainless-steel (SS) coin-cell spacer. This architecture was employed for the extensive electrochemical testing, e.g., cycling and rate performance.

**ADVANCED
SCIENCE NEWS**

www.advancedsciencenews.com

**ADVANCED
MATERIALS**

www.advmat.de
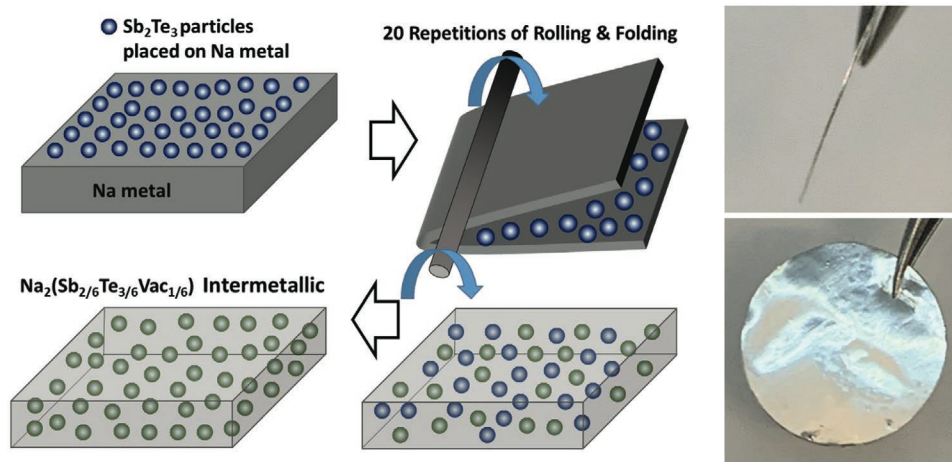
Scheme 1. (Left) Illustration for the fabrication process of sodium–antimony–telluride–Na metallurgical composite, termed NST-Na. The structure was obtained by repeated rolling and folding of Sb_2Te_3 powder and a Na-metal foil. An in-situ-formed electrochemically stable intermetallic NST skeleton supports an electrochemically active Na-metal matrix. (Right) Photographs taken inside the glove box of the 150 μm thick self-standing NST-Na foil.

Configuration 2 has NST-Na or NST being supported by a standard Cu current collector, which is in turn placed on the SS spacer. This configuration was employed for the targeted tests where the specimens that would then undergo postmortem analytical characterization, being better suited removing the NST-Na or NST electrodes from the coin cell and separating them from the collector.
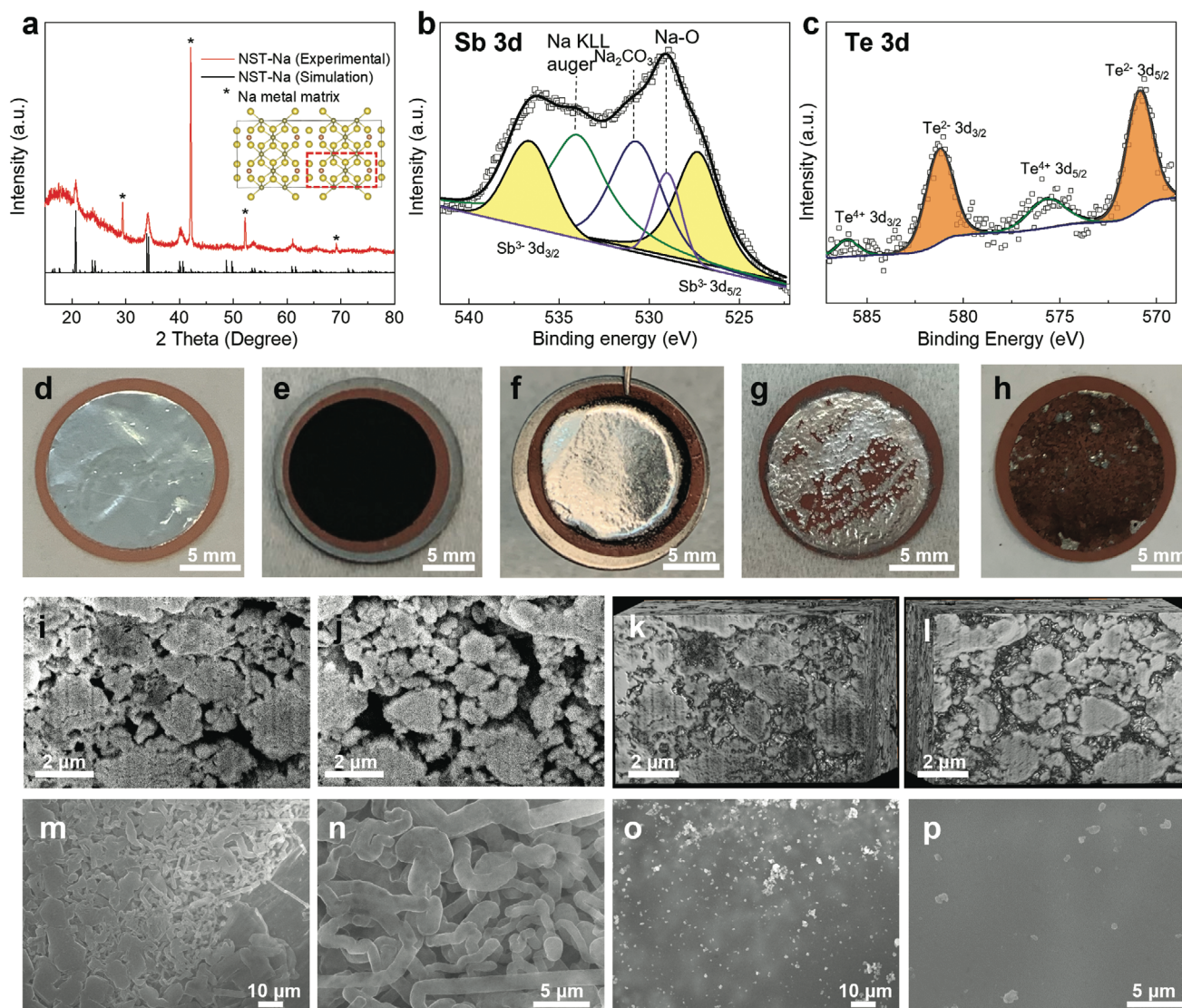
Figure S2a–c in the Supporting Information shows SEM images of the as-received Sb_2Te_3 powder and the associated size distribution of the particles. Using optical stereology methods (Nano Measurer), the average particle diameter was calculated to be 300 nm. It may be observed from the images that there is some agglomeration, where smaller particles are stuck to the surface of the larger ones. Figure S3a in the Supporting Information shows a cross-sectional SEM image of the as-synthesized NST-Na, along with the associated energy-dispersive X-ray spectroscopy (EDXS) elemental maps. It may be observed that NST crystallites are densely and uniformly distributed within the Na-metal matrix. Subsequent FIB cross-sectional SEM tomography results will demonstrate that NST makes a percolated skeleton inside the Na-metal matrix. The NST crystallites are micrometers in their diameter and in their separation from each other. Top-down SEM analysis and the associated EDXS maps of the foil are shown in Figure S3b,c. The images further highlight the geometrically uniform distribution of NST intermetallics within the Na-metal matrix.

The structure of NST was further analyzed by DFT calculations. The ordering of Sb and Te in the NST intermetallic was considered by enumerating many different configurations with the CASM package.[24] Structural enumeration started from the primitive Na_2Te cell, which was optimized in terms of lattice parameters and the atomic positions. The measured XRD patterns shown in **Figure 1**a were directly correlated with DFT modeled lowest energy structures. The obtained structure shown as the inset matches well with the experimental XRD pattern. Details about the structure is given in Figures S4 and S5 in the Supporting Information. It may be observed that the unit cell of $Na_2(Sb_{2/6}Te_{3/6}Vac_{1/6})$ is 3.8% larger than the Na_2Te

cell. The increased volume is due to the partial substitution of Te^{2-} (207 ppm) with larger ionic radius Sb^{3-} (245 pm). It is noteworthy that the reaction between Na and Sb_2Te_3 through mechanical mixing is different from the electrochemical reaction of Sb_2Te_3 with Na. When Sb_2Te_3 electrode is discharged in a cell, two equilibrium binary compounds, Na_2Te and Na_3Sb are formed, with the reaction being reversible.[25] As will be demonstrated, the $Na_2(Sb_{2/6}Te_{3/6}Vac_{1/6})$ intermetallic does not decompose upon charging.

X-ray photoelectron spectroscopy (XPS) was carried out to investigate the chemical valences of Sb and Te in the composite. Figure 1b shows the high-resolution Sb 3d spectrum. The Sb 3d spectrum overlaps with O 1s and Na Auger spectra.[26] The Sb^{3-} $3d_{5/2}$ (527.3 eV) and Sb^{3-} $3d_{3/2}$ (536.7 eV) peaks can be observed along with Na–O (529.0 eV), Na_2CO_3 (530.7 eV), and Na KLL (534.1 eV) peaks. As shown in Figure 1c, there are two pairs of peaks in the high-resolution Te 3d spectrum. The strongest one can be assigned to Te^{2-} $3d_{5/2}$ at 570.8 eV and Te^{2-} $3d_{3/2}$ at 581.2 eV, followed by Te^{4+} (TeO_2) $3d_{5/2}$ at 575.2 eV and Te^{4+} (TeO_2) $3d_{3/2}$ at 585.6 eV. The existence of TeO_2 is ascribed to the slight oxidation on the sample surface, which often appears in the XPS spectra such as Na_2Te.[27] Both Sb^{3-} and Te^{2-} interact with Na^+ to achieve charge neutrality in the compound. Since oxidation states of Sb^{3-} and Te^{2-} are different, for every two Sb^{3-} substitutional anions, there is one Te^{2-} vacancy generated. Therefore, the stoichiometry of NST was confirmed as $Na_2(Sb_{2/6}Te_{3/6}Vac_{1/6})$, agreeing with the DFT results.

As a baseline for structural analysis, Te powder was combined in an identical manner with Na, forming equilibrium Na_2Te. Likewise, equilibrium Na_3Sb was formed when Sb powder was combined with Na. The structures of the composites were analyzed by XRD and DFT simulation. Figure S6a in the Supporting Information shows XRD analysis of baseline as-synthesized metallurgical composites of Na_2Te–Na (NT–Na), Na_3Sb–Na (NS–Na), the fcc Na_2Te structure (Fm-$3m$, No. 225, $a = b = c = 0.7294$ nm), the hcp Na_3Sb structure ($P6_3/mmc$, No. 194, $a = b = 0.5366$ nm, $c = 0.9515$ nm), and the bcc Na-metal matrix (Im-$3m$, No. 229, $a = b = c = 0.4291$ nm).

ADVANCED
SCIENCE NEWS

www.advancedsciencenews.com

ADVANCED
MATERIALS

www.advmat.de

Figure 1. a) XRD analysis of as-synthesized NST-Na along with the DFT simulation of $Na_2(Sb_{2/6}Te_{3/6}Vac_{1/6})$ structure based on archetype fcc Na_2Te. Inset is the representative crystal structure of NST from cluster enumeration and the unit cell is indicated by the red dotted box. Color scheme: Na (yellow), Sb (brown), and Te (green). b,c) High-resolution XPS spectra of NST showing the fitted Sb 3d and Te 3d peaks. d) Photograph of as-fabricated NST-Na anode. e) Photograph of NST after Na was fully stripped from the electrode. f) Photograph of fully stripped NST followed by plating of 2 mAh cm^{-2} capacity. g) Photograph of baseline Cu current collector with a plated capacity of 2 mAh cm^{-2}. h) Photograph of baseline Cu current collector, with Na fully stripped. i,j) FIB cross-sectional SEM images and k,l) FIB-SEM tomography of NST, highlighting its interconnected 3D structure, showing the front views and the back views, respectively. m,n) SEM images of baseline Cu current collector with a plated capacity of 0.5 mAh cm^{-2} at cycle 1. o,p) Same analysis for NST. Testing for (m)–(p) was performed in 1 M $NaPF_6$ in G2 electrolyte.

The experimental XRD pattern for the as-received antimony telluride (Sb_2Te_3) power is shown in Figure S6b in the Supporting Information, indicating that the material has the equilibrium rhombohedral structure ($R3m$, No. 166, $a = b = 0.4262$ nm, $c = 3.0435$ nm). According to Figure S6b in the Supporting Information, Bragg peaks for Sb_2Te_3 are not present in NST-Na, indicating all Sb_2Te_3 has fully reacted with the Na metal.

The structural and compositional evolution during the rolling-folding process was also studied using XRD. As shown in Figure S7 in the Supporting Information, two characteristic peaks of Sb_2Te_3 at 28° and 38° gradually weaken from

the second to the fifth rolling–folding iteration. After the tenth iteration, they fully disappear, demonstrating a complete reaction between Sb_2Te_3 and Na to form NST-Na. The additional 10 iterations were given to further homogenize the distribution of NST particles throughout the foil, with no further change in the XRD patterns being detected. Figure S8a in the Supporting Information displays the XRD patterns of NST-Na with the Sb_2Te_3 to Na weight ratios of 1:4, 1:6, 1:8, and 1:10, corresponding to Sb_2Te_3 weight percentages of 20.0, 14.3, 11.1, and 9.1 wt%. From the patterns it may be concluded that the structure of the metallurgical composites is identical, regardless of the initial Sb_2Te_3 loading.

ADVANCED
SCIENCE NEWS
www.advancedsciencenews.com

ADVANCED
MATERIALS
www.advmat.de

Figure 1d–h investigates the structure and the electrochemical performance of NST-Na and of the baseline Na cells under deep-cycling conditions in 1 M NaPF$_6$ in G2 electrolyte. Figure 1d shows a photograph of the as-fabricated NST-Na anode, taken inside the glove box to prevent the Na metal from oxidizing. For this set of analyses, a Cu foil was employed to support the NST-Na electrode. This allowed for a direct comparison of the stripped Cu collector surfaces with NST-Na versus with the baseline Na, where a Cu foil was always employed. Figure 1e shows a digital photograph of NST after Na was fully stripped from the electrode, highlighting the intact NST layer and the absence of any observable Na metal. The disappearance of Na peak in the XRD analysis as shown in Figure S9 in the Supporting Information further confirms the full stripping of Na metal. Similar results were also obtained for NST-Na electrodes with different initial Sb$_2$Te$_3$ weight loadings. As per the XRD analysis shown in Figure S8b in the Supporting Information, there is no observable difference between the NSTs after Na was fully extracted. This is expected since the structure of the thermodynamically stable NST should not be affected by the Sb$_2$Te$_3$ to Na weight ratio. With relatively more Sb$_2$Te$_3$, however, a higher weight and volume fraction of the NST skeleton is achieved within the composite. This results in relatively more surface area being available to template the plating/stripping of the Na metal, reducing the effective current density. As will be demonstrated, higher NST loading leads to progressively improved electrochemical performance in terms of the plating/stripping overpotentials.

Figure 1f shows a photograph of fully stripped NST followed by plating of 2 mAh cm^{-2} capacity at a current of 1 mA cm^{-2}. The plated metal is macroscopically uniform, the metal surface remaining shiny. The plated morphology and structure of both electrodes will be investigated in more depth in the subsequent figures. Figure 1g provides a photograph of the baseline Cu current collector also with a plated capacity of 2 mAh cm^{-2} at 1 mA cm^{-2}. It may be observed how inhomogeneous the plating of Na metal on a standard Cu current collector really is. The metal is concentrated on the sides of the collector, with macroscopic holes in the film through which the bare Cu is discernable. Apart from the main bulk of the Na film localized toward the upper left and lower bottom portions of the collector, there are also isolated spots of nucleated Na throughout the otherwise bare collector. It may be concluded that Na plating is macroscopically nonuniform from the onset, which explains the early voltage runaway failure observed during cycling of the baseline. Figure 1h shows a photograph of the Cu foil after attempting to strip all the Na metal from its surface. The severe discoloration of the Cu foil is likely associated with the remaining SEI layer which is not removed by the electrode washing procedure. In addition, shiny Na metal is present on the electrode even after it was stripped to the terminal anodic voltage limit of 0.2 V. This is the "dead metal" or "dead sodium", which was not strippable either due to being electrically isolated from the collector, or due to being ionically blocked from dissolving. Both scenarios can be driven by excessive SEI growth. Electrical isolation occurs when the SEI is formed between the metal and the Cu collector, in effect acting as an insulating barrier layer between the two. Ionic insulation occurs if the SEI is thick enough, resistive enough to block the

flow of Na$^+$ from the shrinking metal despite there being sufficient electrical conductance. This combination of SEI and dead metal provides an explanation for the low CE observed with the baseline Na specimen when tested in a half-cell configuration.

Figure S10 in the Supporting Information shows top view and cross-sectional view SEM images and the associated EDXS maps of the poststripped NST supported on the Cu substrate. The Na, Sb, and Te signals are correlated with the irregularly shaped NST particles and there is no evidence for distinct regions containing only Na. Figure S11 in the Supporting Information provides a FIB cross-sectional image of NST and the corresponding EDXS map. A percolated NST skeleton is observed, with the analytical maps showing a homogeneous Na, Sb, and Te distribution throughout. The observed pores in the structure were created after the metallic Na was stripped out. The EDXS analysis gives an atomic ratio of Na:Sb:Te is 6.06:1:1.58, approaching the stoichiometric ratio of 6:1:1.5 in Na$_2$(Sb$_{2/6}$Te$_{3/6}$Vac$_{1/6}$). Figure S12 in the Supporting Information provides TEM images and the associated indexed selected area electron diffraction (SAED) ring pattern of NST. The indexed ring spacings are consistent with the XRD result shown in Figure S9 in the Supporting Information. As expected, the SAED does not contain Na-metal diffraction rings. The 3D structure of NST further elaborated through FIB-SEM tomography. The image shown is reconstructed from a total of 55 FIB cross-sectional slices, each with a thickness of 200 nm (Video S1, Supporting Information).

Figure 1i–l displays FIB cross-sectional SEM tomography of NST, highlighting its interconnected 3D structure, showing the front views and the back views, respectively. The NST skeleton consists of interconnected (percolated) intermetallic particles ranging in size from hundreds of nanometers to several micrometers, many particles likely being polycrystalline agglomerates. It is worth noting that the packing density and the associated porosity of the NST skeleton is related to the initial Sb$_2$Te$_3$ to Na-metal weight ratio. As indicated by the FIB cross-sectional SEM images in Figure S13 in the Supporting Information, the lower Sb$_2$Te$_3$ loadings lead to a looser and more porous NST scaffold. This may be an additional factor explaining the higher overpotentials observed with the lower loadings: During plating, progressively more Na would be plated onto pre-existing Na metal located within the larger pores, rather than directly onto the less available NST surface. Figure S14a in the Supporting Information shows XRD profiles of NST on different substrates (SS spacer, Cu foil) after Na was fully extracted at 1 mA cm^{-2} in 1 M NaPF$_6$ in G2 electrolyte. Figure S14b in the Supporting Information shows an FIB cross-sectional SEM image of NST on the SS spacer. As expected, the structure and morphology of the NST are independent of the type of substrate employed.

Figure 1m–p shows the SEM images of early-stage Na deposition behavior on the Cu supported NST and on the baseline bare Cu collector. The results shown are for cycle 1, with a plated capacity of 0.5 mAh cm^{-2} at the current density of 1 mA cm^{-2}, in 1 M NaPF$_6$ in G2. Curved filament-like dendrites are present on the bare Cu foil even at the first plating cycle. By contrast, the Na plated on NST is planar with a smooth surface. The plated capacity corresponds to 4.4 µm Na film in the ideal planar case, being thinner for the 3D NST support. In the

**ADVANCED
SCIENCE NEWS**

www.advancedsciencenews.com

**ADVANCED
MATERIALS**

www.advmat.de
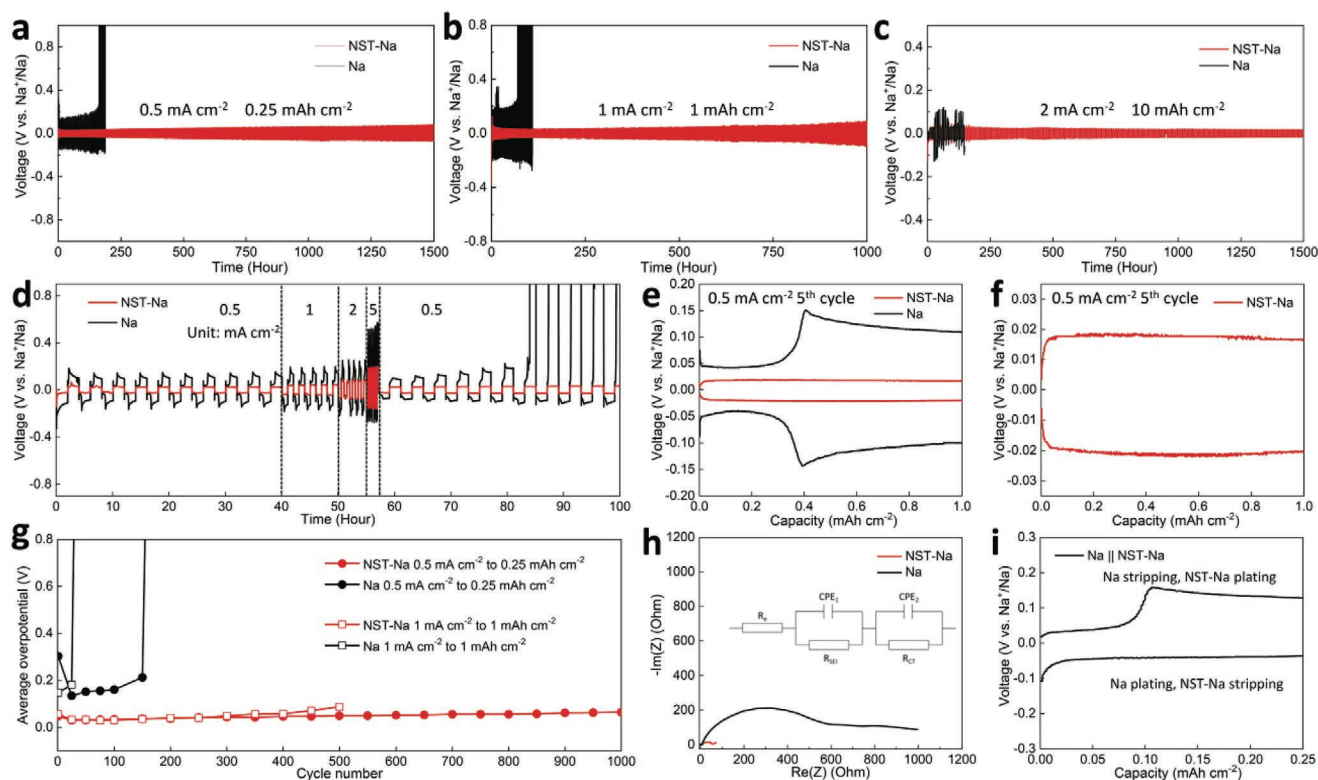
Figure 2. a–i) Electrochemical performance of symmetric cells based on NST-Na and baseline Na. a) Voltage profiles at 0.5 mA cm^{-2} to capacity of 0.25 mAh cm^{-2} per cycle in 1 M NaFSI in EC/DEC. b) Profiles at 1 mA cm^{-2} to capacity of 1 mAh cm^{-2} per cycle, in 1 M NaFSI in EC/DEC. c) Profiles at 2 mA cm^{-2} to capacity of 10 mAh cm^{-2} per cycle, in 1 M NaPF$_6$/G2. d) Rate performance at 0.5, 1, 2, and 5 mA cm^{-2} to 1 mAh cm^{-2} per cycle, in 1 M NaFSI in EC/DEC. e,f) Galvanostatic profile at 0.5 mA cm^{-2} at cycle 5 and associated magnified view, in 1 M NaFSI in EC/DEC. g) Average overpotentials at 0.5 and 1 mA cm^{-2}, in 1 M NaFSI in EC/DEC. h) EIS Nyquist plots after 5 cycles at 0.5 mA cm^{-2} to 1 mAh cm^{-2} per cycle, in 1 M NaFSI in EC/DEC. i) Voltage profile at cycle 5 of asymmetric NST-Na∥Na cells, at 0.5 mA cm^{-2}, in 1 M NaFSI in EC/DEC.

SEM image, the NST is not fully covered by the Na metal, and may be seen protruding onto the surface especially in the top right region of the image. The plated Na is flat and uniform in its morphology, with no dendritic structures present. Analyses were also carried out using the carbonate electrolyte 1 M NaFSI in EC/DEC, also at cycle 1 and 0.5 mAh cm^{-2}. As shown in Figure S15 in the Supporting Information, uniform Na deposition is achieved with NST versus dendrites on the baseline Cu foil. It can therefore be concluded that the marked difference of the early-stage plating behavior with NST versus the baseline is a general feature spanning electrolyte classes.

Figure 2a–i and Figures S16 and S17 in the Supporting Information display the electrochemical performance of symmetric NST-Na∥NST-Na and identically tested baseline cells of Na∥Na, NT–Na∥NT–Na, and NS–Na∥NS–Na. Figure 2a shows these voltage versus time profiles, tested at 0.5 mA cm^{-2} to capacity of 0.25 mAh cm^{-2} per cycle, in 1 M NaFSI in EC/DEC electrolyte. Figure 2b shows the profiles at 1 mA cm^{-2} to 1 mAh cm^{-2} per cycle, in the same electrolyte. As expected in a carbonate electrolyte the baseline Na∥Na cells display early onset of unstable voltage, with significant fluctuations incurring by cycle 162 at 0.5 mA cm^{-2}, and by cycle 35 at 1 mA cm^{-2}. By contrast, the NST-Na∥NST-Na cells remain stable at these rates. They achieve 1500 cycles, 375 mAh cm^{-2} cumulative capacity, and 1000 cycles, 500 mAh cm^{-2} without voltage instability. Figure S16 in

the Supporting Information shows additional cycling data, collected at 0.5 mA cm^{-2} to 2 mAh cm^{-2}, 1 mA cm^{-2} to 0.25 mAh cm^{-2}, and 2 mA cm^{-2} to 1 mAh cm^{-2} in the same electrolyte. Here again, NST-Na displays markedly better performance than the baseline. Table S1 in the Supporting Information compares the plating capacity, DOD, and accumulated capacity of NST-Na∥NST-Na cells with state-of-the-art Na-metal anode literature. It may be observed that from each of the three vantage points, the performance of NST-Na is among the most favorable.

Figure S17 in the Supporting Information shows the voltage profiles of NT–Na∥NT–Na and NS–Na∥NS–Na cells tested at 0.5 mA cm^{-2} to 0.25 mAh cm^{-2} per cycle, also in 1 M NaFSI in EC/DEC. It may be concluded that although the NT–Na and NS–Na composites show improved electrochemical performance (more than doubled and quadrupled cycle life vs baseline Na), they are inferior to NST-Na. This highlights the impact of the ternary NST-Na composite metallurgy in establishing uniform plating and stripping behavior of Na metal. With NST-Na∥NST-Na cells, 1500 mAh cm^{-2} cumulative capacity can be achieved in 1 M NaPF$_6$ in G2. By contrast, the Na∥Na cells become unstable after 25 mAh cm^{-2}, as shown in Figure 2c. Figure S18 in the Supporting Information shows the voltage profiles of NST-Na∥NST-Na with different starting Sb$_2$Te$_3$ to Na-metal ratios, tested at 0.5 mA cm^{-2} to 0.25 mAh cm^{-2} per cycle, in 1 M NaFSI in EC/DEC. The symmetric cells based on

ADVANCED
SCIENCE NEWS

www.advancedsciencenews.com

ADVANCED
MATERIALS

www.advmat.de

electrodes with a higher mass loading of NST exhibit a more stable cycling performance, although all the specimens are superior to the baseline. As mentioned earlier, relatively higher Sb_2Te_3 loading leads to relatively more NST that is available for plating of a given capacity of Na. This should reduce the effective current density and the associated overpotentials. The higher loading NST electrodes also display fewer large pores where the Na metal will accumulate and ultimately plate onto itself. This is another factor in reducing the plating and stripping overpotentials.

Figure 2d shows the rate performance of the symmetric cells, at a current density range of 0.5 to 5 mA cm^{-2}, tested in 1 M NaFSI in EC/DEC. The corresponding plating/stripping time is varied accordingly so as to achieve the targeted 1 mAh cm^{-2} capacity per cycle. It may be observed that the NST-Na‖NST-Na exhibits markedly lower voltage polarization at each of the current densities, the difference versus the baseline increasing with current. The baseline Na‖Na displays unstable voltage at 5 mA cm^{-2} right at the onset, and likewise becomes unstable at cycle 7 when the current is reduced to 0.5 mA cm^{-2}. By contrast NST-Na‖NST-Na cycles through entire current density regime in a stable manner. Figure 2e,f provides expanded views of the fifth cycle galvanostatic curves for NST-Na‖NST-Na and Na‖Na symmetric cells, tested at 0.5 mA cm^{-2} in 1 M NaFSI in EC/DEC. The baseline Na‖Na symmetric cell displays two distinct voltage plateaus. The first plateau at lower voltage with ≈40% of capacity is followed by the second plateau at higher voltage with ≈60% of capacity. The NST-Na‖NST-Na cell does not show this behavior, rather having a much smaller and nondescript single voltage plateau at either plating or stripping.

A Na‖Cu half-cell configuration also tested at 0.5 mA cm^{-2} and 1 mAh cm^{-2} at cycle 5 displays a CE of 40%. That result is shown in Figure S19 in the Supporting Information. The remaining 60% of capacity is lost through the reaction of Na ions with the electrolyte to form additional SEI and the formation of dead metal (as will be demonstrated). The two-plateau stripping and plating profiles of the symmetric Na‖Na cells may now be understood in the context of the half-cell results: The 40% capacity lower voltage plateau corresponds to stripping of the metal deposited in the prior cycle, while the 60% capacity higher voltage plateau corresponds to the necessity to strip the underlying fresh metal to achieve the targeted capacity per cycle. Since the cells are symmetrical, upon plating the working electrode, the same two-stage stripping profile is experienced on the counter electrode. A similar two-stage plateau was also observed in other common carbonate-based electrolytes. Figure S20a in the Supporting Information displays the voltage versus capacity profiles of NST-Na‖NST-Na and Na‖Na symmetric cells at the fifth cycle in 1 M NaClO$_4$ in EC/DEC. With Na‖Na two plateaus are present, the first plateau being at 45% of the total capacity. With NST-Na‖NST-Na tested identically, there is a single flat voltage plateau. Figure S20b in the Supporting Information shows symmetric cells tested at 1 M NaClO$_4$ in EC/PC/FEC. The additive FEC is well-known to stabilize the SEI structure of metal anodes and improve their cycling performance.[28] The improvement of Na‖Na cells with FEC additive can be understood by the elongated first plateau at lower voltage, which accounts for ≈85% of the overall capacity, i.e., 85% CE. This is the highest CE for baseline Na‖Na cells among

all electrolytes tested here. The NST-Na‖NST-Na cell continue to display a single plateau with a relatively lower overpotentials.

Figure 2g plots the average of the plating and stripping overpotentials at every cycle for 0.5 mA cm^{-2} to 1 mAh cm^{-2} per cycle, in 1 M NaFSI in EC/DEC. The panel highlights the major differences in both the cycling stability and the average overpotentials with NST-Na‖NST-Na architecture. Figure 2h displays the electrochemical impedance spectroscopy (EIS) results for the two sets of symmetrical cells after 5 cycles at the same conditions. The inset in the figure shows the model used for fitting the data. The NST-Na‖NST-Na cell has a lower combination of charge transfer resistance and SEI resistance than the Na‖Na cell, being at 54 Ω versus 624 Ω. This is indicative of a thinner, less resistive SEI layer formed with NST-Na‖NST-Na. Figure 2i shows a voltage profile of a purposely configured asymmetric NST-Na‖Na cell, tested analogously. In this case, the Na side experiences a two-stage stripping profile. However, the NST-Na side experiences a single stage voltage profile. The asymmetry in the stripping behavior of the NST-Na versus the baseline Na electrodes is further confirmed. These electrochemical findings will be explained by the microstructural results reported later in the manuscript.

Figure 3 explores the electrochemical performance of NST-Na cells under deep-cycling conditions in 1 M NaPF$_6$ in G2 electrolyte. For this analysis, deep cycling means at 100% DOD, i.e., fully stripped and then fully plated electrodes. This has not been examined in literature for Na-metal anodes, particularly in terms of understanding the cycling versus microstructures in the 100% DOD states. As indicated in the introduction and Table S1 in the Supporting Information, normally thick Na foils are employed for such tasks, with 5% or less of the metal undergoing plating and stripping at each cycle. Examining 100% DOD specimens therefore represents the most aggressive testing regiment in terms of anode volume changes and comes the closest to representing "anodeless"/"anode-free" configurations for full metal batteries where all the active ions are stored in the cathode. Figure 3a shows the voltage versus time data for NST-Na‖NST-Na cells cycled under different DOD at 1 mA cm^{-2}. The active Na was first stripped from the NST-Na electrode (the first step shown in Figure 3a), and then Na was repeatedly plated/stripped. The panel shows incremental increases in DOD going from left to right, starting with 20%, then 40%, 60%, and 80%, and finally 100% corresponding to a plated/stripped capacity of 15 mAh cm^{-2}. One important point worth mentioning is that the amount of NST on each side of the cell stays fixed at 20 wt% of the initial mass loading. As per the XRD analysis in Figure S21 in the Supporting Information, the NST phase is stable during anodic polarization that occurs when stripping, not changing its structure by any detectable measure. This indicates that at 100% DOD, a fixed NST skeleton interspersed with 15 mAh cm^{-2} of Na metal is able to successfully template another 15 mAh cm^{-2} of Na on top of it. The weight percentage of NST on the fully plated side is 11 wt%. On each electrode the NST remains invariant whether the Na metal is stripping or plating.

Aggressive DOD experiments were also carried out in carbonate-based electrolytes. As shown in Figure S22 in the Supporting Information, 92% DOD is achieved in 1 M NaClO$_4$ in EC/PC/FEC, while 72% DOD is achieved in 1 M NaFSI in

ADVANCED
SCIENCE NEWS
www.advancedsciencenews.com

ADVANCED
MATERIALS
www.advmat.de
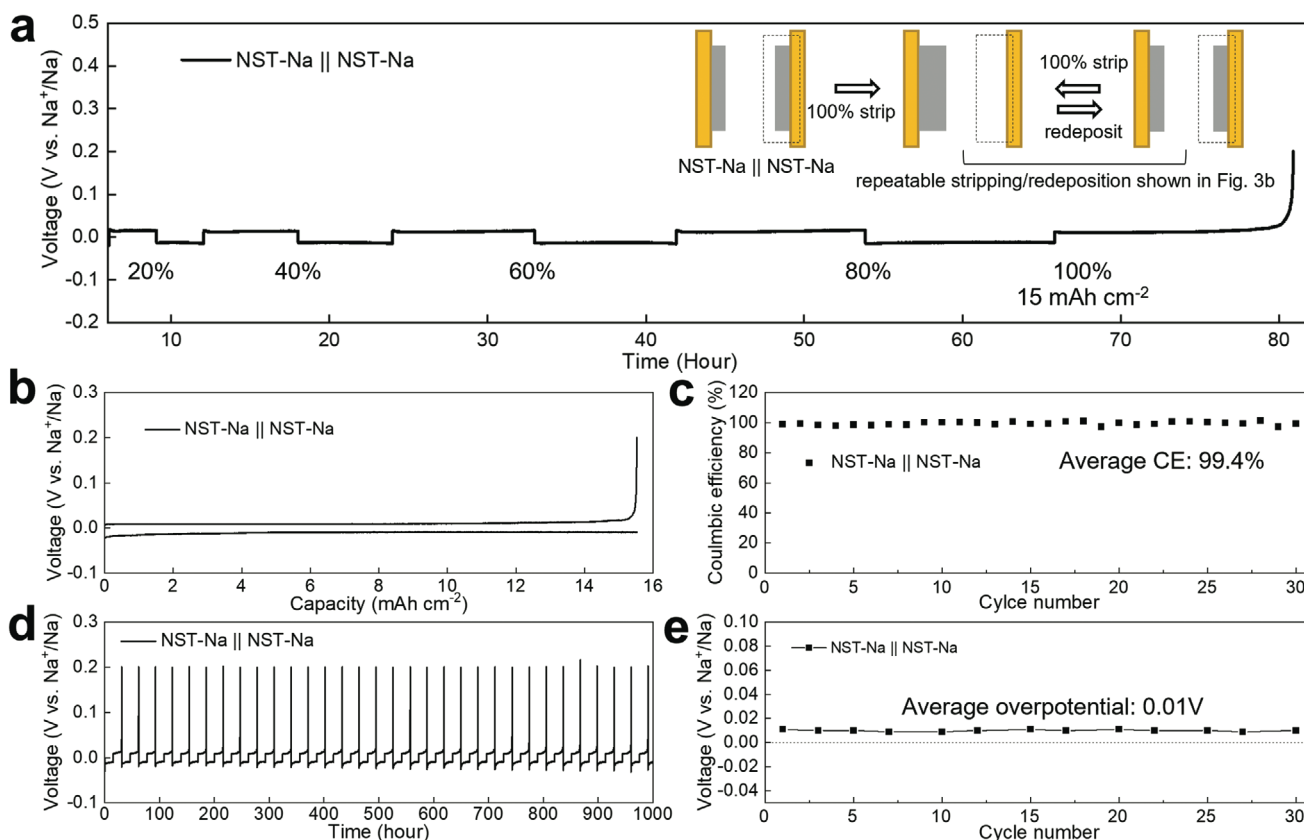
Figure 3. Electrochemical performance of NST-Na cells under deep-cycling conditions in 1 M NaPF$_6$ in G2 electrolyte. a) NST-Na cells cycled under different DOD at 1 mA cm^{-2}. b–e) Voltage profiles, Coulombic efficiencies (CEs), and average plating overpotentials for NST-Na electrode cycled under 100% DOD at 1 mA cm^{-2}. Active Na was first stripped from the NST-Na electrode (the last step shown in (a)), and then Na was repeatedly plated/stripped.

EC/DEC. By contrast, baseline Na can only cycle at 37% and 52% DOD before it short-circuits. Those results are shown in Figure S23a,b in the Supporting Information. As shown in Figure S23c in the Supporting Information, even in the ether-based electrolyte, baseline Na can only achieve 90% DOD. Figure 3b–e displays voltage profiles, CE values, and average plating overpotentials for NST-Na electrode cycled under 100% DOD at 1 mA cm^{-2}. Figure S24 in the Supporting Information shows similar tests but at more aggressive current densities of 3 and 5 mA cm^{-2}. It may be observed that at 100% DOD the NST-Na cells remain stable with cycling, displaying an average CE of 99.4% at 1 mA cm^{-2} after 1000 h. It also exhibits stable cycling profiles over 500 h at 100% DOD, tested at 3 and 5 mA cm^{-2}, with average CEs of 99.3% and 99.1%. Such voltage stability and relatively high CE has not been reported for Na-metal anodes undergoing complete plating and stripping at every cycle.

Sputter-down XPS was employed to further understand the SEI structure in NST-Na and the baseline Na. These results are shown in **Figure 4**a–h. The specimens were analyzed after five cycles at 0.5 mA cm^{-2} with a capacity 1 mAh cm^{-2} in 1 M NaFSI in EC/DEC. The integral areas of the individual peaks were obtained, allowing for an estimate of the normalized content of each component. This is presented in a form of bar charts in Figure 4d for NST-Na and Figure 4h for Na. For both electrodes,

the SEI mainly consists of Na$_2$CO$_3$, Na$_2$O, and NaF. The ratio of NaF component is slightly higher in the SEI for NST-Na. Overall the SEI composition-phase content is analogous for both electrodes, indicating the NST does not substantially affect the SEI chemistry per se. The key differences are then in the initial SEI thickness and its cycling-induced growth. This is quantitatively supported by the EIS results, and qualitatively by the light optical observations of the initial stripped Cu surface. It will also be quantitatively substantiated by the cryo-FIB and cryo-TEM analysis shown in the next set of figures.

Figure 5 presents SEM, cryo-FIB cross-sectional SEM, and cryo-TEM analysis comparing NST-Na versus Na in the plated condition. Samples underwent 5 cycles at 0.5 mA cm^{-2} with a plated capacity of 1 mAh cm^{-2} per cycle in 1 M NaFSI in EC/DEC. Figure 5a–d highlights analysis of NST-Na, while Figure 5e–h shows comparable analysis for Na. Figure 5a,e shows top-view SEM images. Figure 5b–d,f–h shows SEM images and EDXS maps of cryo-FIB lift out NST-Na and baseline Na specimens. Figure 5i,j provides cryo-TEM images of the cross-sections of NST-Na in the plated condition. Figure 5k,l displays this analysis for Na, with arrows highlighting the porosity in the metal. There is a striking difference in the structure and the morphology of the plated metal for the two specimens. For the case of NST-Na, the plated metal is dense, being free from pores and from imbedded SEI. The surface morphology

**ADVANCED
SCIENCE NEWS**
www.advancedsciencenews.com

**ADVANCED
MATERIALS**
www.advmat.de
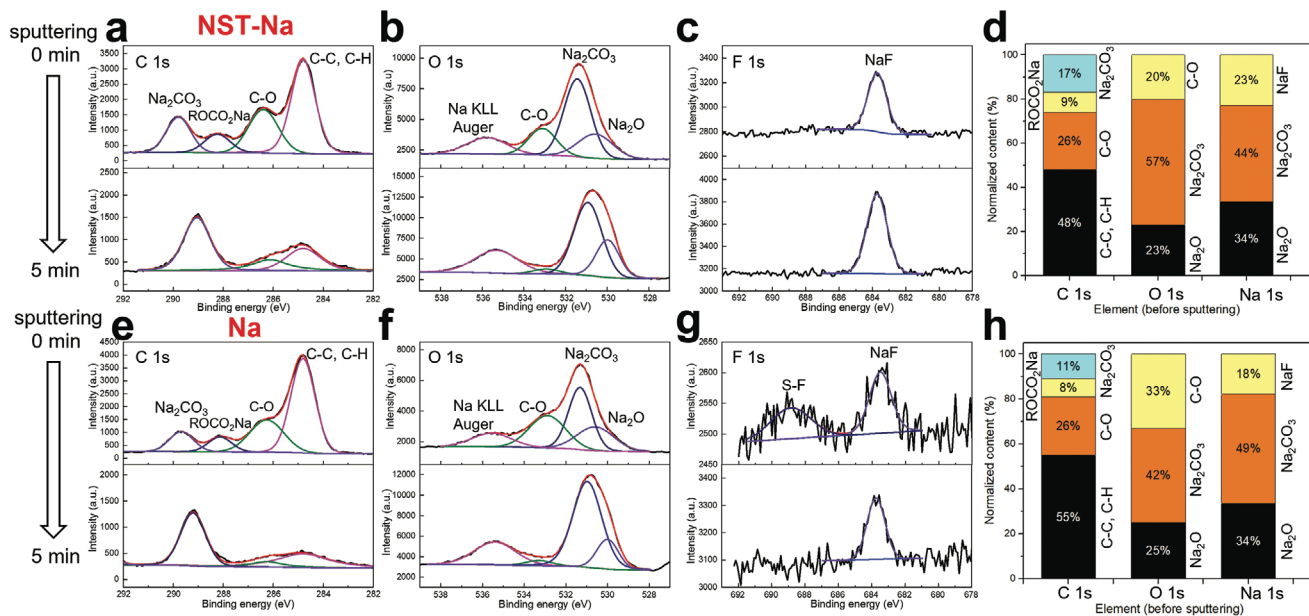
Figure 4. XPS spectra comparing the SEI for fifth cycle plated surfaces of NST-Na versus baseline Na in 1 M NaFSI in EC/DEC. a–d) NST-Na, fitted C 1s, O 1s, and F 1s spectra and bar charts showing the relative percentage of different species in the SEI. e–h) Same analysis but for baseline Na.

of NST is flat, with no evidence of dendrites. The metal is free from nanoporosity, as shown in the higher resolution TEM images. By contrast, the baseline Na electrode is effectively a three-phase sponge: Through the entire structure the plated metal is interspersed with the SEI. Micrometer-scale pores are present everywhere throughout the plated structure, being
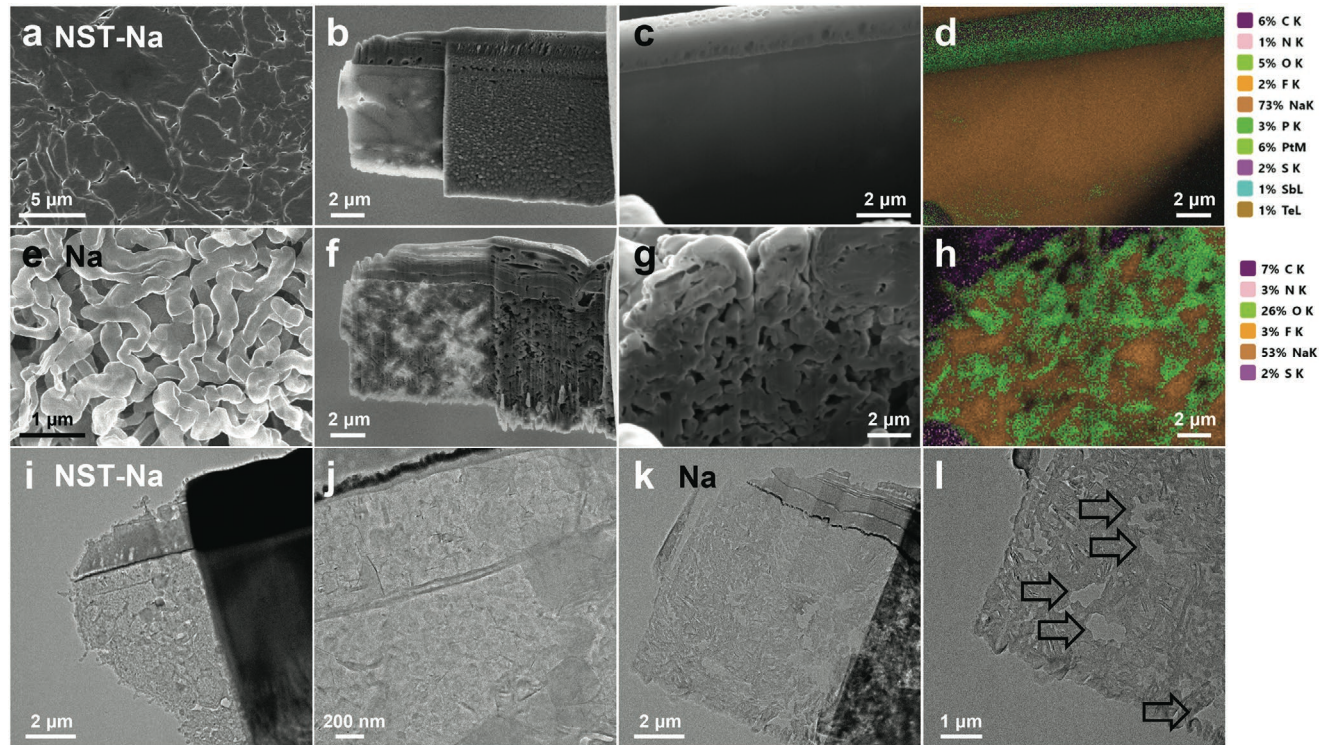

Figure 5. Microscopic analysis comparing NST-Na versus Na in the plated condition (1 M NaFSI in EC/DEC, 5 cycles at 0.5 mA cm^{-2} with a plated capacity of 1 mAh cm^{-2} per cycle). a) Top-view SEM image of the postcycled NST-Na. b) Cryo-FIB lift out specimen. c,d) Cryo-FIB cross-sectional SEM image and EDXS map of the postcycled NST-Na. e–h) Same analysis but for baseline Na. i,j) Cryo-TEM images of the postcycled NST-Na. k,l) Same analysis but for Na, with arrows highlighting the porosity in the metal.

ADVANCED
SCIENCE NEWS
www.advancedsciencenews.com

ADVANCED
MATERIALS
www.advmat.de

visible in the cross-sectional SEM and in the cross-sectional TEM (arrowed) images. This triphasic structure is developed early in cycling and is fundamentally different from the classical view of dendrites as isolated protrusions emanating from a uniform metal foil. The extensive SEI formation throughout the electrode explains with the 40% CE observed at cycle 1. Figures S25–S27 in the Supporting Information show SEM images comparing the deposition morphology for NST-Na versus bare Na in various plated conditions. These samples were analyzed after 1 cycle at 1 mA cm^{-2}, with plating capacities of 5, 10, and 26 mAh cm^{-2}, in 1 M NaFSI in EC/DEC. The observed structures are consistent at the three conditions: dense relatively smooth metal for NST-Na versus a porous dendritic structure for baseline Na.

Full battery cell testing was performed to further evaluate the feasibility of NST-Na electrodes. The cells were based on Na$_3$V$_2$(PO$_4$)$_3$ (NVP) or sulfur (S)-based cathodes combined with NST-Na or Na. Three-electrode electroanalytic work was performed to further understand the performance, the details being provided in the experimental. **Figure 6**a shows the voltage profiles of NST-Na‖NVP and Na‖NVP cells at 1C (1C equals to 118 mA g^{-1} based on the mass of NVP) in 1 M NaFSI in EC/DEC electrolyte. Figure 6b displays three electrode analysis showing the voltage of NVP cathode and the Na anode. Figure 6c

compares the cycling stability of NST-Na‖NVP and Na‖NVP. In carbonate electrolyte, Na‖NVP two-electrode cell shows two discharge plateaus. The first of which gives a capacity of about 40 mAh g^{-1} and is present at ≈3.34 V, followed by the second plateau with 60 mAh g^{-1} at ≈3.24 V. The voltage of NVP cathode and Na anode was measured using a three-electrode cell. During discharge, the voltage of the NVP cathode (working electrode) displays a single plateau, while Na anode (counter electrode) exhibits two plateaus. This is in accordance with the voltage profile of the Na‖Na symmetrical cells discussed previously. The second discharge plateau in the full battery is due to the Na anode polarization, in turn as a result of its poor CE and the need to strip fresh Na metal to compensate for loss of active ions. While two stage plateaus have been reported previous for NVP versus Na metal,[18] this is the first explicit explanation for this behavior. When NVP is coupled with NST-Na, the two-electrode cell shows a single discharge plateau at ≈3.34 V. This is due to the low overpotential and high CE stripping behavior of NST-Na, which utilizes almost all the previously plated Na. The single high-voltage discharge voltage enables an increase of 8.5% in the specific energy of the cell.

Figure S28a in the Supporting Information displays the rate performance of NST-Na‖NVP and Na‖NVP full cells. Stepwise increasing the current densities from 0.2C, 0.5C, 1C, 2C,
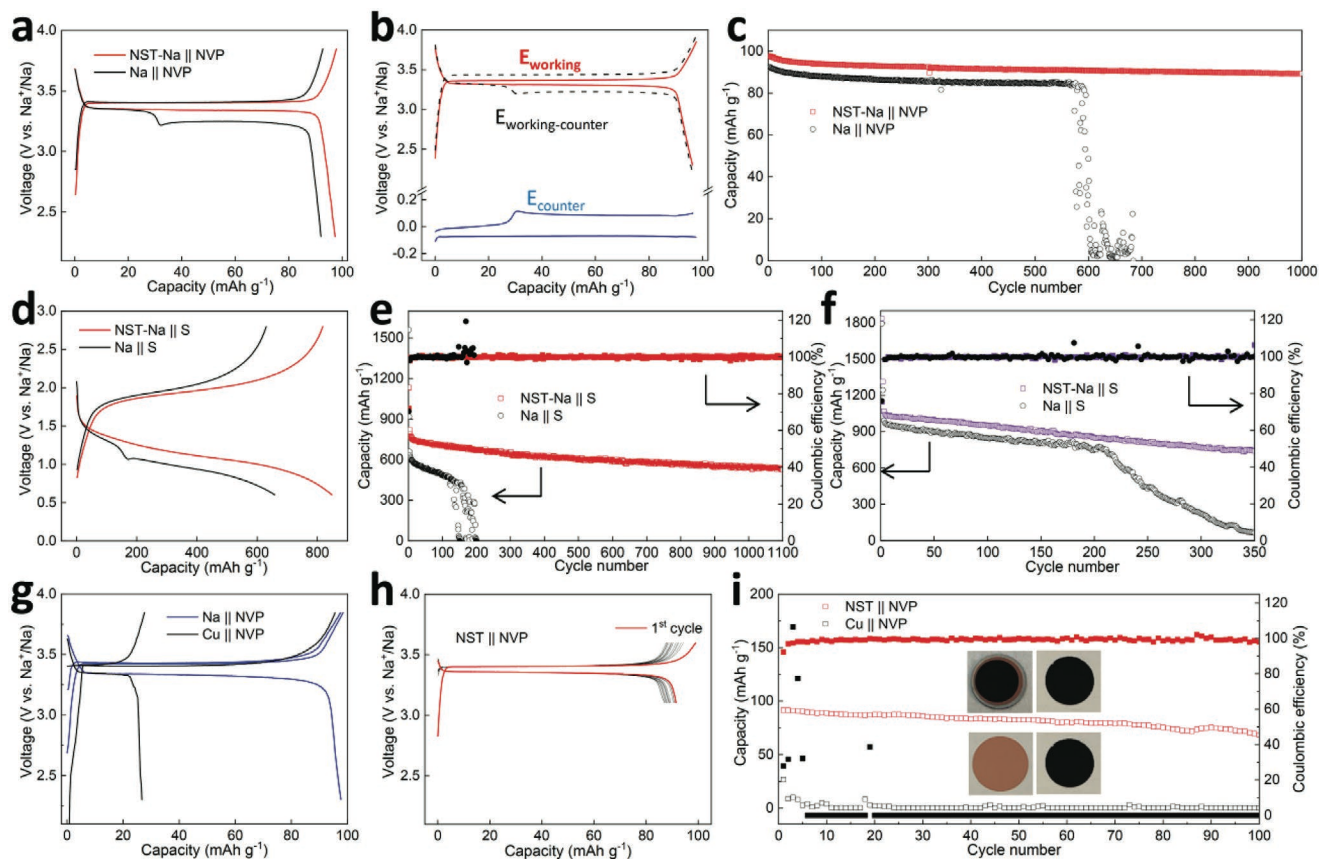
Figure 6. a) Voltage profiles of NST-Na‖NVP and Na‖NVP cells in 1 M NaFSI in EC/DEC electrolyte at 1C. b) Three-electrode analysis showing voltage of NVP cathode and Na anode. c) Cycling stability of NST-Na‖NVP and Na‖NVP cells at 1C. d) Selected voltage profiles of NST-Na‖S and Na‖S cells at 0.5C in 1 M NaFSI in EC/DEC. e) Cycling stability and CE of NST-Na‖S and Na‖S at 0.5C in 1 M NaFSI in EC/DEC. f) Cycling stability and CE of NST-Na‖S and Na‖S cells at 0.5C in 1 M NaClO$_4$ in EC/PC/FEC. g) Voltage profiles of Na‖NVP and Cu‖NVP at 1C in 1 M NaPF$_6$ in G2. h,i) Voltage profiles and cycling performance of an anode-free cell with an NVP cathode (source of Na) and NST versus baseline Cu collector at 1C in 1 M NaPF$_6$ in G2.

**ADVANCED
SCIENCE NEWS**

www.advancedsciencenews.com

**ADVANCED
MATERIALS**

www.advmat.de

5C, 10C, 15C to 20C, the NST-Na‖NVP cell delivers reversible capacities of 109, 105, 105, 103, 101, 97, 93, 90, and 87 mAh g^{-1}, respectively. When the current is switched from 20C back to 0.2C, the reversible capacity is restored to the original level. At every current density, the baseline Na‖NVP exhibits a lower capacity. The NST-Na‖NVP cell can be stably cycled for over 1000 cycles at 1C with 91% capacity retention and an average CE of 99.9%. Figure S29a in the Supporting Information provides the specific energy of the cells. NST-Na‖NVP delivers a specific energy of 296 Wh kg^{-1} after 1000 cycles at a specific power of 380 W kg^{-1}. In contrast, Na‖NVP can be cycled less than 600 times with a fluctuating CE, as shown in Figure S29b in the Supporting Information. As shown in Figure S29c in the Supporting Information, when cycled at an extremely fast rate of 10C, the CE of NST-Na‖NVP remains quite high after 1000 cycles. Table S2 in the Supporting Information compares the rate capability and cycling behavior of NST-Na‖NVP versus literature-reported NVP-based cells with modified Na anodes. It may be concluded that the electrochemical performance of NST-Na‖NVP is among the most favorable.

Sodium–sulfur batteries are exciting because of their high theoretical energy and low cost.[21b,c,29] Figure 6d provides selected voltage profiles of NST-Na‖S and Na‖S at 0.5C (1C equals to 1675 mA g^{-1} based on the mass of S) in 1 M NaFSI in EC/DEC. Figure 6e gives the cycling stability and CE of NST-Na‖S and Na‖S cells. Figure S30 in the Supporting Information displays selected voltage profiles of NST-Na‖S and Na‖S cells in 1 M NaClO$_4$ in EC/PC/FEC. Figure 6f shows the cycling stability and CE of NST-Na‖S and Na‖S cells at 0.5C in 1 M NaClO$_4$ in EC/PC/FEC. For Na–S, the crossover of polysulfides results a relatively low cycle life.[21a] Therefore, comparable performance to NVP cells is not expected, since no custom separators, elaborate electrolytes, etc., were employed. Overall, however, the cycling performance is noticeably improved when employing NST-Na. The cycling life increases from 150 with baseline Na to greater than 1000 cycles with NST-Na, its CE remaining at over 99%. When FEC-containing electrolyte was employed, the capacity of Na–S cells was boosted as well. However, cells with bare Na electrodes still suffered from severe capacity decay after 200 cycles. Those with NST-Na exhibited markedly more stable cycling performance. The baseline Na–S cells display two discharge plateaus in both electrolytes after cycle 1, but they are not quite identical: The second plateau in FEC-containing electrolyte (0.7 V) appears at a lower voltage than that in non-FEC-containing electrolyte (1.05 V), corresponding to a longer first stripping plateau of Na anode. By contrast, NST-Na‖S cell exhibits single plateau in both electrolytes. The different discharge processes between NST-Na‖S and Na‖S cells result from the distinct anode stripping behaviors as per the previous discussion. The lower polarizations in NST-Na‖S cells also contribute to their greater performance. Figure S28b in the Supporting Information shows the rate performance of NST-Na‖S and Na‖S cells. Results demonstrate that the NST-Na‖S cell outperforms the Na‖S cell, the difference increasing with current density. For example, at 5C the NST-Na‖S cell delivers a reversible capacity of 495 mAh g^{-1}, while the baseline Na‖S cell only achieves 191 mAh g^{-1}.

"Anode-free"/"anodeless" metal batteries are attractive due to reduced manufacturing cost, reduced need for Li/Na/K metal,

increased specific energy and volumetric energy, as well as improved safety.[16a,30] Since in the ideal case there is no ion reservoir apart from what is in the cathode, CEs approaching 100% are crucial. Figure 6g shows voltage profiles of Na‖NVP and Cu‖NVP in an anodeless configuration. Figure 6h,i provide voltage profiles and cycling performance of an anode-free cell with an NVP cathode (source of Na) and NST versus baseline Cu collector. Fully stripped NST-Na anode was employed as the NST current collector, the desodation being performed prior to cell assembly. The first charge capacity of a Cu‖NVP cell is almost the same as that of Na–NVP cell (95 mAh g^{-1} vs 97 mAh g^{-1}). However only 27 mAh g^{-1} is recovered for Cu–NVP, indicating a CE of 30%. The anode-free cell using NST gives a cycle 1 CE of 92.3% and a steady-state cycling CE of upward of 99.7%. SEM and EIS analysis were performed to further elucidate the differences between Cu‖NVP and NST‖NVP after the first charge (plating) and after the first discharge (stripping). As shown in Figure S31 in the Supporting Information, the SEM images show that dead metal with dendritic features remains on the stripped Cu surface. By contrast, there is no discernible Na left on the NST surface. Figure S32 in the Supporting Information provides the EIS analysis on the Cu‖NVP and NST‖NVP cells at different charge–discharge states. There is a notable difference at the first discharge state. The combination of charge transfer resistance and SEI resistance of a Cu‖NVP is larger than that of an NST‖NVP, being 609 and 317 Ω, respectively. These results agree well with the analytical and electroanalytical findings for the symmetric and the half-cells.

The enhanced early-stage wettability of Na on the NST surface was examined by DFT calculations. If Na clusters are more thermodynamically stable than Na atoms, early-stage wetting behavior will favor 3D islands rather than atomically thin continuous films. This would naturally lead to dendrites as the film thickness increases. If Na atoms are more stable as compared to Na clusters, the initially plated film will cover the surface uniformly. This scenario does not exclude the possibility of Stransk–Krastanov type dewetting away from the interface during later stages of deposition. However there is little evidence for such behavior with NST supports. The binding energies of Na atoms and Na clusters on the (100) fcc NST surface were calculated and compared to (111) fcc Cu, (110) bcc Na, and (110) fcc Na$_2$Te. The Na$_2$Te was treated as a baseline reference model for NST because of the similarity in their structure. From surface energy calculations (Table S3, Supporting Information), the Cu (111) surface has the lowest surface energy as compared to Cu (110) and Cu (200), these findings agreeing with prior reports.[31] The binding energies were calculated in two configurations: a) Na clusters and b) individual Na atoms. Since it is not known at what Na coverage dendrites first form, cases considered ranged from single atoms to Na clusters with 4–5 atoms. Clusters that were larger in size were too demanding computationally to calculate in practical time frames. On NST and baseline NT surfaces, there is a preference for Na atoms to disperse on the surface. For clusters of 4–5 atoms, there is a clear energetic difference for wetting as compared to clustering. The structures of Na$_4$/Na$_5$ clusters and four/five individual Na atoms on the respective surfaces are shown in Figures S33 and S34 in the Supporting Information. As discussed, a relatively stronger binding energy of individual Na atoms as compared

**ADVANCED
SCIENCE NEWS**
www.advancedsciencenews.com

**ADVANCED
MATERIALS**
www.advmat.de

Table 1. Binding energies for multiple sodium atoms and sodium clusters on the relevant surfaces.

Binding energy per Na [eV]	Four Na atoms	Na$_4$ cluster	Five Na atoms	Na$_5$ cluster
(111) fcc Cu	−1.21	−1.21	−0.67	−0.69
(100) fcc NST	0.01	0.12	0.05	0.11
(110) bcc Na	0.19	0.10	0.16	0.06
(110) fcc Na$_2$Te	0.17	0.23	0.19	0.27

to clusters indicates the propensity to deposit uniformly on a given surface.

The binding energy of the Na$_4$ cluster, Na$_5$ cluster, four and five sodium atoms are shown in **Table 1**. Outcomes with the most positive binding energy are the least thermodynamically stable. On the Cu (111) surface, the four/five individual Na atoms and Na$_4$/Na$_5$ clusters are almost equally stable, indicating there is minimal energetic preference for early-stage islands versus early-stage planar films. This is perhaps the most meaningful outcome of the simulation. It indicates that the experimentally observed early stage plated film morphology is kinetically determined, being influenced by factors as the heterogeneity of the Na-ion flux through the liquid (electrolyte wetting) and through the solid (SEI). With NST, four and five Na atoms are significantly more stable than the clusters, indicating that there is a thermodynamic driving force for complete coverage of the support during early-stage plating. Interestingly, on preexisting Na metal, the individual atoms are less stable than the clusters. This implies a thermodynamic propensity for roughening of the Na-metal surface during ongoing film growth. To some extent this is observed even with NST, where the film morphology is not perfectly planar, especially at higher capacity. It would be difficult to separate these thermodynamic roughening effects from kinetic factors that also influence the film surface morphology. The baseline Na$_2$Te surface results yield more stable Na atoms as compared to clusters, though the energetic difference is not as significant as with NST. As discussed previously, Na$_2$Te is known to decompose during anodic polarization through a conversion reaction, making it a structurally unstable support. Therefore, the uniqueness of NST lies both in the relatively high thermodynamic stability that groups of Na atoms display on its surface and in its own thermodynamic stability that resists decomposition during extended cycling.

Scheme 2 summarizes the electrochemical stabilization effect of NST comparing it to the baseline Na. The schematic treats a scenario where there is 100% DOD, analogous to the configuration shown in Figure 1d–h. At plating cycle 1, the wetting behavior of the Na metal on the Cu substrate is poor. Rather than forming a conformal film, a macroscopically heterogenous island structure is formed. Such metal coverage leads to a likewise geometrically nonuniform SEI on the electrolyte-exposed surfaces. There is also the formation of "dead metal" upon cycle one stripping, with additional dead metal likely being formed at subsequent cycles. During cycling the SEI is never fully stable, as indicated by the poor CE of the half-cells and of the 100% DOD cells, as well as by the impedance values obtained from EIS. From the onset of cycling, the plating overpotentials of the baseline Na are higher than for NST-Na, with
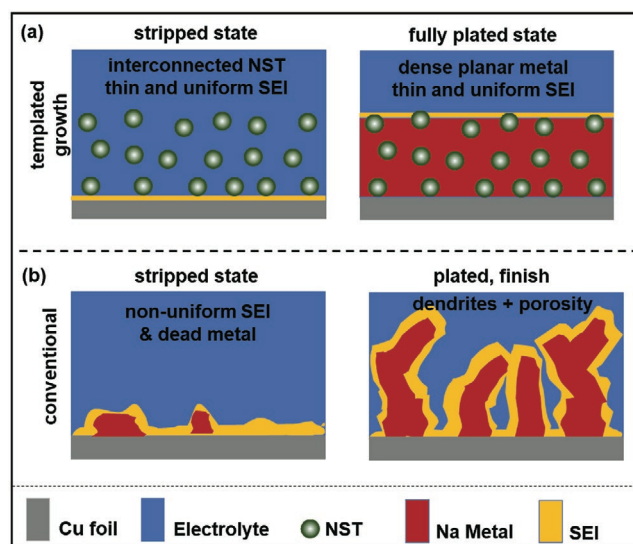
Scheme 2. Illustration of NST enhancement effect on the plating and stripping behavior. a) Role of NST on uniform plating/stripping of Na metal. b) Baseline Cu foil with coarse and irregular SEI from the onset and the formation of dead metal upon stripping.

their difference increasing with cycle number. Relatively higher overpotentials have been theoretically linked to a transition from planar metal growth to island metal growth.[32] A thickening SEI will therefore promote even worse wetting at the subsequent cycle. A deleterious synergy results, where poor metal wetting, increasing overpotentials, and SEI growth become self-amplifying. This leads to a triphasic microstructure observed, consisting of curved Na-metal filaments that are interspersed with SEI and with pores.

3. Conclusion

Sodium-metal batteries (SMBs, NMBs) are hindered by nonuniform plating/stripping of the anode with unstable SEI and potentially catastrophic dendrite growth. Here, a repeated cold rolling and folding method was employed to fabricate a metallurgical composite of thermodynamically stable (as per DFT simulations) sodium antimony telluride Na$_2$(Sb$_{2/6}$Te$_{3/6}$Vac$_{1/6}$) intermetallic crystallites that are densely dispersed in Na metal, termed "NST-Na." This new intermetallic skeleton allowed for state-of-the-art electrochemical performance in both carbonate and ether electrolytes. For example, NST-Na achieved 100% DOD (15 mAh cm^{-2}) at 1 mA cm^{-2} with CE of 99.4% for 1000 h plating/stripping time. Coupled with NVP or sulfur-based cathodes, improved energy, Coulombic efficiency, and cycling are demonstrated. The cell lifetime of the NST-Na∥sulfur battery is increased from 150 to over 1000 cycles. An anode-free cell consisting of an NST anode collector and an NVP cathode was cycled with a capacity loss of only 0.23% per cycle. At cycle 1, NST-Na plates uniformly and strips completely. Baseline Na plates nonuniformly including formation of filament-like dendrites clustered in macroscopic islands. The stripped Cu surface contains macroscopic islands of shiny dead metal that is not electrochemically active enough to be removed. Cryo-TEM

analysis on cryo-FIB cross-sections combined with XPS demonstrate that cycled NST-Na is dense and pore-free, flat on its surface with a stable SEI. The cycled baseline bulk microstructure is triphasic; all the metal is form of curved dendritic filaments that are interspersed with SEI and with pores. A mechanistic explanation of these combined results is put fourth, being directly supported by DFT analysis. One key scientific takeaway is that templated growth is necessary for electrochemical stability of Na metal and that dendritic growth is the default on a standard foil.

Supporting Information

Supporting Information is available from the Wiley Online Library or from the author.

Conflict of Interest

The authors declare no conflict of interest.

Data Availability Statement

The data that support the findings of this study are available from the corresponding author upon reasonable request.

[1] a) B. Sun, P. Xiong, U. Maitra, D. Langsdorf, K. Yan, C. Wang, J. Janek, D. Schröder, G. Wang, *Adv. Mater.* **2020**, *32*, 1903891; b) Y. Zhao, K. R. Adair, X. Sun, *Energy Environ. Sci.* **2018**, *11*, 2673; c) S. Guo, J. Yi, Y. Sun, H. Zhou, *Energy Environ. Sci.* **2016**, *9*, 2978; d) W. Luo, L. Hu, *ACS Cent. Sci.* **2015**, *1*, 420.

[2] a) Y. Liang, H. Dong, D. Aurbach, Y. Yao, *Nat. Energy* **2020**, *5*, 646; b) C. Yang, K. Fu, Y. Zhang, E. Hitz, L. Hu, *Adv. Mater.* **2017**, *29*, 1701169; c) G. J. Rees, D. S. Jolly, Z. Ning, T. J. Marrow, G. E. Pavlovskaya, P. G. Bruce, *Angew. Chem., Int. Ed.* **2021**, *60*, 2110.

[3] a) D. Lin, Y. Liu, Y. Cui, *Nat. Nanotechnol.* **2017**, *12*, 194; b) P. Zou, Y. Sui, H. Zhan, C. Wang, H. L. Xin, H. M. Cheng, F. Kang, C. Yang, *Chem. Rev.* **2021**, *121*, 5986; c) B. Lee, E. Paek, D. Mitlin, S. W. Lee, *Chem. Rev.* **2019**, *119*, 5416; d) H. Wang, E. Matios, J. Luo, W. Li, *Chem. Soc. Rev.* **2020**, *49*, 3783; e) W. Zhou, Y. Li, S. Xin, J. B. Goodenough, *ACS Cent. Sci.* **2017**, *3*, 52; f) L. Lin, L. Suo, Y. Hu, H. Li, X. Huang, L. Chen, *Adv. Energy Mater.* **2021**, *11*, 2003709.

[4] a) S. Wei, S. Choudhury, J. Xu, P. Nath, Z. Tu, L. A. Archer, *Adv. Mater.* **2017**, *29*, 1605512; b) J. Zheng, M. H. Engelhard, D. Mei, S. Jiao, B. J. Polzin, J. G. Zhang, W. Xu, *Nat. Energy* **2017**, *2*, 17012.

[5] W. Luo, C. F. Lin, O. Zhao, M. Noked, Y. Zhang, G. W. Rubloff, L. Hu, *Adv. Energy Mater.* **2017**, *7*, 1601526.

[6] a) S. Chen, J. Zheng, D. Mei, K. S. Han, M. H. Engelhard, W. Zhao, W. Xu, J. Liu, J. G. Zhang, *Adv. Mater.* **2018**, *30*, 1706102; b) M. D. Tikekar, S. Choudhury, Z. Tu, L. A. Archer, *Nat. Energy* **2016**, *1*, 16114; c) D. Zhang, S. Wang, B. Li, Y. Gong, S. Yang, *Adv. Mater.* **2019**, *31*, 1901820; d) K. Yan, Z. Lu, H. W. Lee, F. Xiong, P. C. Hsu, Y. Li, J. Zhao, S. Chu, Y. Cui, *Nat. Energy* **2016**, *1*, 16010; e) J. Wu, Z. Rao, X. Liu, Y. Shen, C. Fang, L. Yuan, Z. Li, W. Zhang, X. Xie, Y. Huang, *Adv. Mater.* **2021**, *33*, 2007428; f) C. Yan, X. B. Cheng, Y. X. Yao, X. Shen, B. Q. Li, W. J. Li, R. Zhang, J. Q. Huang, H. Li, Q. Zhang, *Adv. Mater.* **2018**, *30*, 1804461.

[7] a) G. G. Eshetu, G. A. Elia, M. Armand, M. Forsyth, S. Komaba, T. Rojo, S. Passerini, *Adv. Energy Mater.* **2020**, *10*, 2000093; b) C. Bao, B. Wang, P. Liu, H. Wu, Y. Zhou, D. Wang, H. Liu, S. Dou, *Adv. Funct. Mater.* **2020**, *30*, 2004891.

[8] a) Y. Xu, Y. Zhu, Y. Liu, C. Wang, *Adv. Energy Mater.* **2013**, *3*, 128; b) N. Yabuuchi, K. Kubota, M. Dahbi, S. Komaba, *Chem. Rev.* **2014**, *114*, 11636.

[9] a) Y. Okamoto, *J. Phys. Chem. C* **2013**, *118*, 16; b) C. Luo, Y. Zhu, Y. Wen, J. Wang, C. Wang, *Adv. Funct. Mater.* **2014**, *24*, 4082.

[10] a) S. Choudhury, S. Wei, Y. Ozhabes, D. Gunceler, M. J. Zachman, Z. Tu, J. H. Shin, P. Nath, A. Agrawal, L. F. Kourkoutis, T. A. Arias, L. A. Archer, *Nat. Commun.* **2017**, *8*, 898; b) H. J. Yoon, N. R. Kim, H. J. Jin, Y. S. Yun, *Adv. Energy Mater.* **2018**, *8*, 1701261; c) Z. W. Seh, J. Sun, Y. Sun, Y. Cui, *ACS Cent. Sci.* **2015**, *1*, 449; d) W. Liu, P. Li, W. Wang, D. Zhu, Y. Chen, S. Pen, E. Paek, D. Mitlin, *ACS Nano* **2018**, *12*, 12255.

[11] a) A. Wang, X. Hu, H. Tang, C. Zhang, S. Liu, Y. W. Yang, Q. H. Yang, J. Luo, *Angew. Chem., Int. Ed.* **2017**, *56*, 11921; b) H. Wang, C. Wang, E. Matios, W. Li, *Nano Lett.* **2017**, *17*, 6808; c) R. Rodriguez, K. E. Loeffler, S. S. Nathan, J. K. Sheavly, A. Dolocan, A. Heller, C. B. Mullins, *ACS Energy Lett.* **2017**, *2*, 2051; d) P. Shi, S. Zhang, G. Lu, L. Wang, Y. Jiang, F. Liu, Y. Yao, H. Yang, M. Ma, S. Ye, X. Tao, Y. Feng, X. Wu, X. Rui, Y. Yu, *Adv. Energy Mater.* **2020**, *11*, 2003381; e) Y. Deng, J. Zheng, A. Warren, J. Yin, S. Choudhury, P. Biswal, D. Zhang, L. A. Archer, *Adv. Energy Mater.* **2019**, *9*, 1901651.

[12] P. Bai, J. Li, F. R. Brushett, M. Z. Bazant, *Energy Environ. Sci.* **2016**, *9*, 3221.

[13] a) X. Zheng, H. Fu, C. Hu, H. Xu, Y. Huang, J. Wen, H. Sun, W. Luo, Y. Huang, *J. Phys. Chem. Lett.* **2019**, *10*, 707; b) S. Wang, W. Cai, Z. Sun, F. Huang, Y. Jie, Y. Liu, Y. Chen, B. Peng, R. Cao, G. Zhang, S. Jiao, *Chem. Commun.* **2019**, *55*, 14375; c) X. Zheng, Z. Gu, X. Liu, Z. Wang, J. Wen, X. Wu, W. Luo, Y. Huang, *Energy Environ. Sci.* **2020**, *13*, 1788; d) X. Hu, E. Matios, Y. Zhang, C. Wang, J. Luo, W. Li, *Angew. Chem., Int. Ed.* **2021**, *60*, 5978.

[14] a) Z. Tu, S. Choudhury, M. J. Zachman, S. Wei, K. Zhang, L. F. Kourkoutis, L. A. Archer, *Nat. Energy* **2018**, *3*, 310; b) Y. Zhao, L. V. Goncharova, A. Lushington, Q. Sun, H. Yadegari, B. Wang, W. Xiao, R. Li, X. Sun, *Adv. Mater.* **2017**, *29*, 1606663; c) Z. Xu, J. Yang, T. Zhang, L. Sun, Y. Nuli, J. Wang, S. Hirano, *Adv. Funct. Mater.* **2019**, *29*, 1901924; d) C. Xiao, R. Usiskin, J. Maier, *Adv. Funct. Mater.* **2021**, *31*, 2100938; e) L. Zhang, X. Zhu, G. Wang, G. Xu, M. Wu, H. K. Liu, S. X. Dou, C. Wu, *Small* **2021**, *17*, 2007578;

f) M. Zhu, G. Wang, X. Liu, B. Guo, G. Xu, Z. Huang, M. Wu, H. K. Liu, S. X. Dou, C. Wu, *Angew. Chem., Int. Ed.* **2020**, *59*, 6596.

[15] a) Y. Zhang, C. Wang, G. Pastel, Y. Kuang, H. Xie, Y. Li, B. Liu, W. Luo, C. Chen, L. Hu, *Adv. Energy Mater.* **2018**, *8*, 1800635; b) F. Wu, J. Zhou, R. Luo, Y. Huang, Y. Mei, M. Xie, R. Chen, *Energy Storage Mater.* **2019**, *22*, 376; c) Q. Wang, C. Zhao, X. Lv, Y. Lu, K. Lin, S. Zhang, F. Kang, Y. S. Hu, B. Li, *J. Mater. Chem. A* **2019**, *7*, 24857; d) Y. Zhao, X. Yang, L. Y. Kuo, P. Kaghazchi, Q. Sun, J. Liang, B. Wang, A. Lushington, R. Li, H. Zhang, X. Sun, *Small* **2018**, *14*, 1703717; e) S.-S. Chi, X.-G. Qi, Y.-S. Hu, L.-Z. Fan, *Adv. Energy Mater.* **2018**, *8*, 1702764; f) T. Li, J. Sun, S. Gao, B. Xiao, J. Cheng, Y. Zhou, X. Sun, F. Jiang, Z. Yan, S. Xiong, *Adv. Energy Mater.* **2020**, *11*, 2003699; g) X. Zheng, P. Li, Z. Cao, W. Luo, F. Sun, Z. Wang, B. Ding, G. Wang, Y. Huang, *Small* **2019**, *15*, 1902688; h) X. He, S. Jin, L. Miao, Y. Cai, Y. Hou, H. Li, K. Zhang, Z. Yan, J. Chen, *Angew. Chem., Int. Ed.* **2020**, *59*, 16705.

[16] a) A. P. Cohn, N. Muralidharan, R. Carter, K. Share, C. L. Pint, *Nano Lett.* **2017**, *17*, 1296; b) S. Tang, Z. Qiu, X. Y. Wang, Y. Gu, X. G. Zhang, W. W. Wang, J. W. Yan, M. S. Zheng, Q. F. Dong, B. W. Mao, *Nano Energy* **2018**, *48*, 101; c) B. Sun, P. Li, J. Zhang, D. Wang, P. Munroe, C. Wang, P. H. L. Notten, G. Wang, *Adv. Mater.* **2018**, *30*, 1801334; d) S. Tang, Y. Y. Zhang, X. G. Zhang, J. T. Li, X. Y. Wang, J. W. Yan, D. Y. Wu, M. S. Zheng, Q. F. Dong, B. W. Mao, *Adv. Mater.* **2019**, *31*, 1807495; e) Y. Xu, C. Wang, E. Matios, J. Luo, X. Hu, Q. Yue, Y. Kang, W. Li, *Adv. Energy Mater.* **2020**, *10*, 2002308; f) J. Wu, P. Zou, M. Ihsan-Ul-Haq, N. Mubarak, A. Susca, B. Li, F. Ciucci, J. K. Kim, *Small* **2020**, *16*, 2003815.

[17] X. Zheng, W. Yang, Z. Wang, L. Huang, S. Geng, J. Wen, W. Luo, Y. Huang, *Nano Energy* **2020**, *69*, 104387.

[18] W. Liu, Z. Chen, Z. Zhang, P. Jiang, Y. Chen, E. Paek, Y. Wang, D. Mitlin, *Energy Environ. Sci.* **2021**, *14*, 382.

[19] a) M. E. Lee, S. Lee, J. Choi, H. J. Jin, S. Han, Y. S. Yun, *Small* **2019**, *15*, 1901274; b) J. Qian, B. D. Adams, J. Zheng, W. Xu, W. A. Henderson, J. Wang, M. E. Bowden, S. Xu, J. Hu, J. G. Zhang, *Adv. Funct. Mater.* **2016**, *26*, 7094; c) J. G. Zhang, *Nat. Energy* **2019**, *4*, 637.

[20] Y. Lee, J. Lee, J. Lee, K. Kim, A. Cha, S. Kang, T. Wi, S. J. Kang, H. W. Lee, N. S. Choi, *ACS Appl. Mater. Interfaces* **2018**, *10*, 15270.

[21] a) X. Xu, D. Zhou, X. Qin, K. Lin, F. Kang, B. Li, D. Shanmukaraj, T. Rojo, M. Armand, G. Wang, *Nat. Commun.* **2018**, *9*, 3870; b) Y. Wang, D. Zhou, V. Palomares, D. Shanmukaraj, B. Sun, X. Tang, C. Wang, M. Armand, T. Rojo, G. Wang, *Energy Environ. Sci.* **2020**, *13*, 3848; c) Y. X. Wang, B. Zhang, W. Lai, Y. Xu, S. L. Chou, H. K. Liu, S. X. Dou, *Adv. Energy Mater.* **2017**, *7*, 1602829.

[22] a) L. Schafzahl, I. Hanzu, M. Wilkening, S. A. Freunberger, *ChemSusChem* **2017**, *10*, 401; b) P. M. L. Le, T. D. Vo, H. Pan, Y. Jin, Y. He, X. Cao, H. V. Nguyen, M. H. Engelhard, C. Wang, J. Xiao, J. G. Zhang, *Adv. Funct. Mater.* **2020**, *30*, 2001151.

[23] a) Y. Fang, R. Lian, H. Li, Y. Zhang, Z. Gong, K. Zhu, K. Ye, J. Yan, G. Wang, Y. Gao, Y. Wei, D. Cao, *ACS Nano* **2020**, *14*, 8744; b) X. Zhang, F. Hao, Y. Cao, Y. Xie, S. Yuan, X. Dong, Y. Xia, *Adv. Funct. Mater.* **2021**, *31*, 2009778.

[24] a) CASM v0.2.1, https://github.com/prisms-center/CASMcode (accessed: August 2020); b) CASM v0.2.1, https://doi.org/10.5281/zenodo.546148 (accessed: August 2020).

[25] Z. Yang, J. Sun, J. Ni, Z. Zhao, J. Bao, S. Chen, *Energy Storage Mater.* **2017**, *9*, 214.

[26] a) N. Zhao, C. Li, X. Guo, *Phys. Chem. Chem. Phys.* **2014**, *16*, 15646; b) G. V. Zhuang, B. S. Mun, P. N. Ross Jr., *J. Chem. Phys.* **2009**, *131*, 084502.

[27] J. Zhang, Y. X. Yin, Y. G. Guo, *ACS Appl. Mater. Interfaces* **2015**, *7*, 27838.

[28] a) S. Komaba, T. Ishikawa, N. Yabuuchi, W. Murata, A. Ito, Y. Ohsawa, *ACS Appl. Mater. Interfaces* **2011**, *3*, 4165; b) R. Dugas, A. Ponrouch, G. Gachot, R. David, M. R. Palacin, J. M. Tarascon, *J. Electrochem. Soc.* **2016**, *163*, A2333.

[29] A. Y. S. Eng, V. Kumar, Y. Zhang, J. Luo, W. Wang, Y. Sun, W. Li, Z. W. Seh, *Adv. Energy Mater.* **2021**, *11*, 2003493.

[30] A. P. Cohn, T. Metke, J. Donohue, N. Muralidharan, K. Share, C. L. Pint, *J. Mater. Chem. A* **2018**, *6*, 23875.

[31] R. Tran, Z. Xu, B. Radhakrishnan, D. Winston, W. Sun, K. A. Persson, S. P. Ong, *Sci. Data* **2016**, *3*, 160080.

[32] W. Liu, P. Liu, D. Mitlin, *Chem. Soc. Rev.* **2020**, *49*, 7284.